Geophys. J. Int. (2008) **175,** 1154–1168 doi: 10.1111/j.1365-246X.2008.03957.x

An upper-mantle *S*-wave velocity model for Northern Europe from Love and Rayleigh group velocities

Christian Weidle and Valérie Maupin

Department of Geosciences, University of Oslo, PO Box 1047, 0316 *Oslo, Norway. E-mail: christian.weidle@geo.uio.no*

Accepted 2008 August 29. Received 2008 August 29; in original form 2008 June 3

SUMMARY

A model of upper-mantle *S*-wave velocity and transverse anisotropy beneath northwestern Europe is presented, based on regional surface wave observations. Group velocities for both Love and Rayleigh surface waves are measured on waveform data from international and regional data archives (including temporary deployments) and then inverted for group velocity maps, using a method accounting for Fresnel zone sensitivity. The group velocity variations are larger than in global reference maps, and we are able to resolve unprecedented details. We then apply a linear inversion scheme to invert for local 1-D shear wave velocity profiles which are consequently assembled to a 3-D model. By choosing conservative regularization parameters in the 2-D inversion, we ensure the smoothness of the group velocity maps and hence of the resulting 3-D shear wave speed model. To account for the different tectonic regimes in the study region and investigate the sensitivity of the 1-D inversions to inaccuracies in crustal parameters, we analyse inversions with different reference models of increasing complexity (pure 1-D, 3-D crust/1-D mantle and pure 3-D). We find that all inverted models are very consistent at depths below 70 km. At shallower depths, the constraints put by the reference models, primarily Moho depth which we do not invert for, remain the main cause for uncertainty in our inversion. The final 3-D model shows large variations in *S*-wave velocity of up to ± 12 per cent. We image an intriguing low-velocity anomaly in the depth range 70–150 km that extends from the Iceland plume beneath the North Atlantic and in a more than 400 km wide channel under Southern Scandinavia. Beneath Southern Norway, the negative perturbations are around 10 per cent with respect to ak135, and a shallowing of the anomaly is indicated which could be related to the sustained uplift of Southern Scandinavia in Neogene times. Furthermore, our upper-mantle model reveals good alignment to ancient plate boundaries and first-order crustal fronts around the triple junction of the Baltica-Avalonia–Laurentia collision in the North Sea.

Key words: Surface waves and free oscillations; Seismic anisotropy; Seismic tomography; Europe.

1 INTRODUCTION

Todays northwestern Europe formed at early Palaeozoic times from the collision of three entities: Baltica, Avalonia and Laurentia (Cocks & Torsvik 2005). Baltica, which had accreted to its final geometry in late Proterozoic (around 1 Ga) docked to the Avalonian plate in Ordovician–Silurian time (443 Ma) and shortly after collided with the Laurentia plate, closing the Iapetus ocean in the Caledonian orogeny. The sutures between these entities are only partly observable today (Fig. 1). The Iapetus suture (ISZ) can be traced in Ireland, mainland Great Britain and offshore into the North Sea (e.g. England 1995; Landes *et al.* 2006; Tomlinson *et al.* 2006), but the track is lost northeastwards due to the overprinting of the North Atlantic opening some 400 Ma later. The suture between Avalonia and Baltica starts off in the west in the North Sea as the Thor Zone (ThS), joining beneath Denmark with the Sorgenfrei-Tornquist Zone (STZ) to form the Tornquist-Teisseyre Zone which is an integral part of the Trans-European-Suture-Zone (TESZ) between Baltica and Variscan Europe (e.g. Winchester 2002).

Apart from the ocean–continent transition, a major topographic feature of Northern Europe is the high topography along the west coast of Scandinavia (Fig. 2) that follows the trend of the Caledonian orogeny west of the Caledonian Thrust Front (CTF). The former Caledonian mountain range collapsed in the second half of the Palaeozoic (380 Ma) and can therefore not explain this high topography. The region underwent then several phases of rifting and uplift including a major phase of uplift in Triassic–Jurassic times (220 Ma) (e.g. Smelror *et al.* 2007). Further extensional phases led

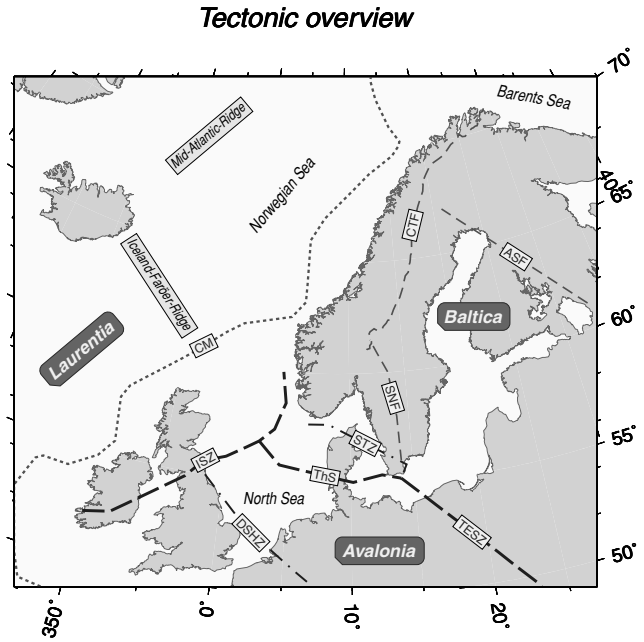

Figure 1. Schematic tectonic overview. Thick black dashed lines indicate identified suture zones of Avalonia, namely Iapetus suture (ISZ) to Laurentia and the Trans-European-Suture-Zone (TESZ) and Thor Suture (ThS) to Baltica. Alternative boundaries (thinner dash–dot lines) include the Dowsing-South Hewett Fault Zone (DSHZ) and the Sorgenfrei-Tornquist Zone (STZ). The grey dotted line marks todays continental margin (CM, following 500 m bathymetry) and grey dashed lines internal deformation fronts within the Baltica plate related to Archean-Svecofennian (ASF) (∼2 Ga), Svecofennian–Sveconorwegian (SNF) (∼1 Ga) and Caledonian (CTF) (∼450–500 Ma) orogenies.

to differential uplift, among them doming of the North Sea, generating topographic contrasts and eventually leading to continental breakup in Early Eocene (52 Ma), in connection with the opening of the mid-Atlantic. Major uplift phases in Palaeogene (Northern Norway) and Neogene (Southern Norway) led to todays topography of western Scandinavia. The mechanisms for these latest uplift phases are not completely understood and several models are under debate. A mantle source supporting the uplift at least in Southern Norway is conceivable due to the long wavelength of the topography in this region, and an asthenospheric diapirism model was proposed by Rohrman & van der Beek (1996) to explain Neogene uplift around the Northeast Atlantic margin. Ebbing & Olesen (2005) used gravimetric anomalies and geoid heights to analyse different scenarios for isostatic compensation of the Northern and Southern Scandes by low-density material, combined with different degrees of lithospheric flexure rigidities. They concluded that the two mountain ranges may arise from two different mechanisms, the Northern Scandes being possibly sustained by low density at rather shallow crustal depth and the Southern Scandes being possibly related to deeper mantle structures. But they also concluded that the lack of appropriate knowledge on the crust and upper-mantle structure in the region is a major problem to constrain geodynamical models to explain the uplift.

Previous seismological images of the upper mantle for the region from global tomography (e.g. Bijwaard *et al.* 1998) or regional tomography (e.g. Pilidou *et al.* 2005) have imaged low velocities beneath the Atlantic and under Southern Scandinavia. However, these features were either too coarse to reveal geometric details or too close to the resolution limit to allow for serious interpretation. On a smaller scale, the coverage of high-resolution seismic models for the upper mantle beneath Northern Europe is sparse. There are a number of regional tomographic studies for regions bordering Scandinavia, for example, Iceland plume domain, Central Europe or the Arctic region. In Scandinavia itself, such regional models are available only for smaller regions like the Tornquist-Teisseyre Transition Zone in Denmark/Southern Sweden (TOR project, e.g. Shomali *et al.* 2002), Finland (SVEKALAPKO, e.g. Sandoval *et al.* 2004) and very recently for a profile through Sweden (Eken *et al.* 2007).

One of the more recent studies on upper-mantle structure beneath Norway is the work by Bannister *et al.* (1991) who analysed arrival times of *Pn* and *Sn* waves and found relatively low *P*- and *S*-wave velocities in the upper mantle underneath the regions of maximum topography in Southern Norway. Low velocities in the shallow upper mantle beneath Southern Norway have also been mapped earlier by Husebye *et al.* (1986) in a *P*-wave tomography of Southern Scandinavia. While the large-scale studies struggle with a limited resolution in the region, the regional body wave studies from the

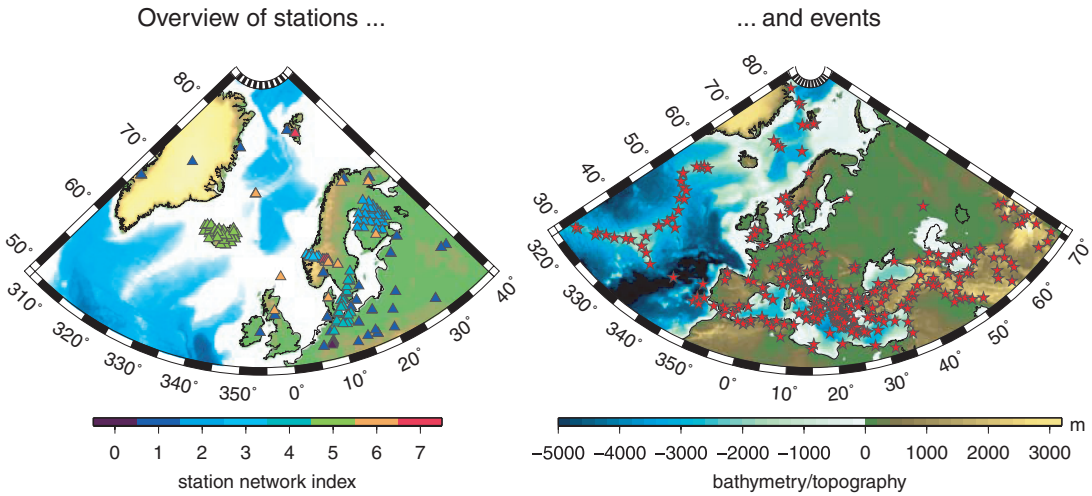

Figure 2. Overview of stations (left-hand side) and events (right-hand side) used in this study. The station network code is as follows: 0—EIFEL network, 1—GSN/GEOFON permanent stations, 2—SVEKALAPKO network, 3—CENMOVE network, 4—TOR network, 5—HOTSPOT network, 6—NORSAR archive, 7—NORSAR arrays in Hamar and Spitzbergen.

late 1980s were limited to land areas and the Skagerrak region and also had their limits in vertical resolution. These observations, although some 15–20 yr old are, however, still widely used for tectonic interpretations of the uplift history of the Northeast Atlantic margin.

Over the last decades, new seismic stations were permanently or temporarily installed in and around this region, allowing for new tomographic studies with enhanced resolution. We present here a regional tomographic analysis of group velocity data for this region.

2 DATA ACQUISITION AND PROCESSING

Following the same strategy as Levshin *et al.* (2007) in their study on the greater Barents Sea region to the north of our study area, we collected broad-band data from the early 1970s until 2005 from stations in Northern Europe. None of the data from Levshin *et al.* were used in this study, but we retrieved surface wave observations from the same data archives.

We extracted event parameters for earthquakes along the mid-Atlantic ridge south of Iceland to the Azores triple junction, from the entire Mediterranean region and eastward into Iran. The limiting box for the event selection process was set to 40°W–70°E/30°–85°N, in which we employed three searches:

(1) From the NEIC catalogue, the initial 3512 events with magnitude ≥5 in the period 1997 until 2005 May were reduced to 199 events by clustering the events in bins of 2° × 2° degree, only keeping the strongest event in each bin.

(2) From NORSAR's regional event catalogue for the period 1992–2003, we extracted all events in the region within a distance of 2000 km from the NORSAR network and magnitudes above 4.

(3) 35 selected events in the time period 1978–2005 within regional distances (especially from Scandinavia, around the north, Baltic and Norwegian Sea) were added manually.

After cleansing the list from eventually duplicate entries, we ended up with 359 events to process (Fig. 2).

Based on this event list, we harvested the GSN and GEOFON data centres for available data in the region. In addition, we also included data from temporary deployments in Iceland (HOTSPOT experiment), Scandinavia (CENMOVE, TOR and SVEKALAPKO experiments) as well as data from the EIFEL PLUME Experiment in Central Europe. Similar to the data search described in Levshin *et al.* (2007), we also included data from regional station and network operators not directly accessible via internet request and which were kindly made accessible through NORSAR data centre.

The waveform data were deconvolved from the instrument response and group velocities for Love and Rayleigh waves, measured in the period range 10–200 s using the frequency–time analysis (FTAN) software (Ritzwoller & Levshin 1998). The manual measurements were processed similarly as described in Section 2 of Levshin *et al.* (2007), including outlier rejection, implementation of EHB catalogue (Engdahl *et al.* 1998) for source parameters and event clustering (detailed in Ritzwoller & Levshin 1998). From the clustering analysis, we estimate the uncertainty of our measurements between 0.2–0.3 km s^{-1}. Correction for source group delays could not be applied since focal mechanisms are not available for many of our analysed events. According to Levshin *et al.* (1999), we can, however, safely ignore these corrections since we are dealing mostly with shallow events and small to intermediate periods.

Given our station/event distribution, we achieve a fairly homogeneous coverage of large parts of Central and Northern Europe (Fig. 3). The ray path density maps, calculated in a 1° × 1° degree grid reveal that the actual highest path density is in Central Europe and a corridor extending northwestwards towards Iceland.

Due to the intermediate size of the majority of the analysed events, the histogram of number of observations per period shows a maximum at around 25–30 s, with the majority of data between 16 and 80 s (Fig. 4).

We also present azimuthal coverage maps in Fig. 3 which are calculated at each gridpoint as squared sums of azimuthal path density $\chi = \frac{(\sum f_i)^2}{\sum f_i^2}$. f_i is the number of Gaussian paths in the ith azimuthal bin (similar to the description by Barmin *et al.* 2001) and we applied 18° bins, hence χ will vary between 1 (poorest coverage) and 10 (optimal coverage). We will discuss these maps in the context of resolution in the following section.

3 2-D INVERSION OF GROUP VELOCITIES

To invert our group velocity observations for 2-D group velocity maps, we followed the procedure described by Barmin *et al.* (2001) and Ritzwoller *et al.* (2002) which includes a geometrical Fresnel zone approximation to account for sensitivity of surface waves off the great circle path. We inverted both Love and Rayleigh wave group velocities for a set of periods between 16 and 150 s on a 1° × 1° degree grid. As reference maps for the inversion, we used global 2-D group velocity maps, kindly provided by A. Levshin from Colorado University in Boulder. After testing and thoroughly inspecting inversions for different parameter combinations (see Barmin *et al.* 2001, for details) and the respective trade-off curves (Fig. 4), we chose to apply a rather conservative set of damping parameters. In a later step, we will use the resulting group velocity maps as input data for localized depth inversions; to ensure smoothness in the final shear wave velocity model, a rather smooth model with larger residuals is therefore preferable to a model with too strong perturbations.

Figs 5 and 6 present maps of Rayleigh (Fig. 5) and Love (Fig. 6) wave group velocities at selected periods, together with the reference background model and the estimated resolution (calculated as described in Barmin *et al.* 2001). As Rayleigh and Love wave group velocity maps are obtained independently, it is interesting to notice that they are, in general, very consistent with each other. For example, Love wave group velocities at 25 s and Rayleigh wave group velocity at 18 s, which have maximum sensitivity at about the same depth, show very similar lateral variations. The two maps at the same period (18 s), on the other hand, nicely illustrate the differing depth sensitivity of both wave types. Notice also the similarities between the Love wave velocity map at 70 s period and the Rayleigh wave velocity map at 40 s period. The group velocity maps reveal, in general, a large number of details as compared to the reference model (Figs 5 and 6). They show an increase in geometrical details as well as stronger contrasts. Note the large scales of ±20 per cent for 18 s periods and ±15 per cent at 80 s, which are, however, not unusual for group velocity maps at regional scale (e.g. Villaseñor *et al.* 2001; Huang *et al.* 2003; Yanovskaya & Kozhevnikov 2003; Feng *et al.* 2004). The first-order features of relative velocity variations are preserved from the reference model and to a large extent emphasized, for example, the low velocities beneath Iceland or the general east–west contrast of oceanic and continental regimes.

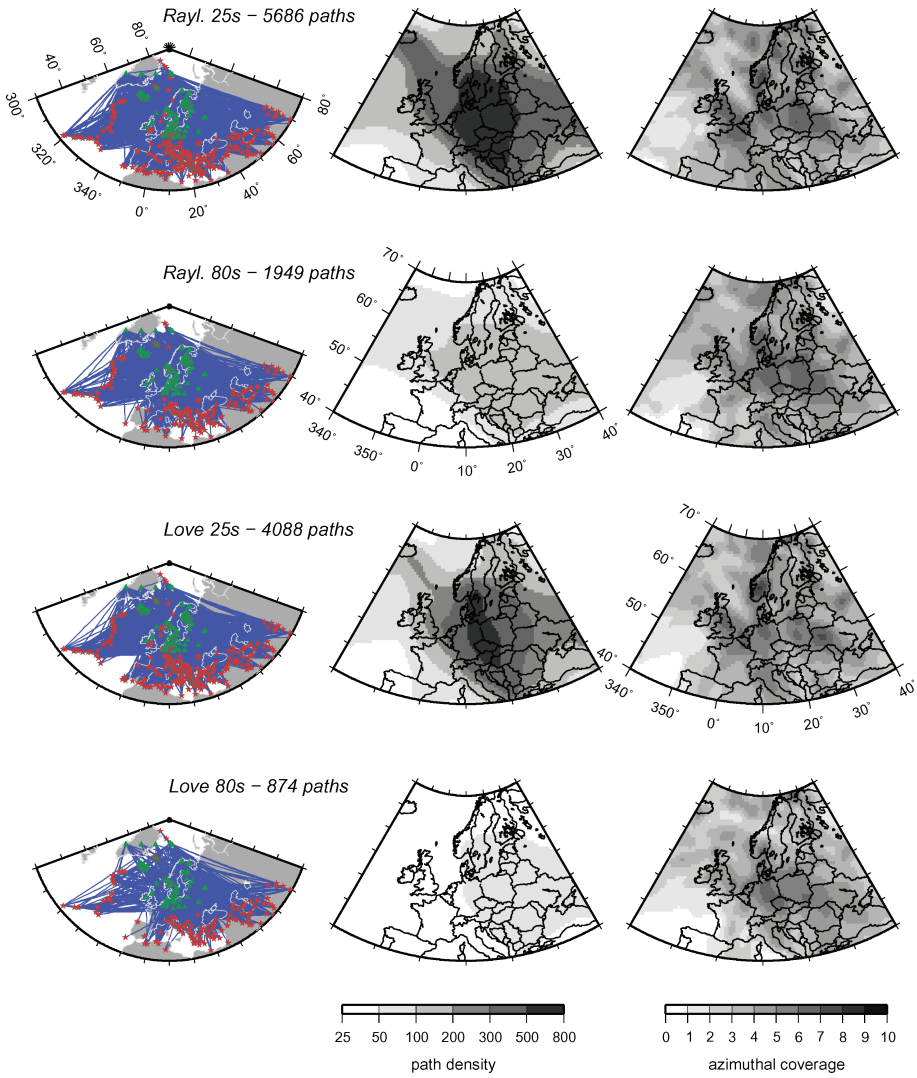

Figure 3. Data coverage, path density and azimuthal coverage at periods 25 and 80 s for Rayleigh and Love waves. Left-hand column shows the ray paths (blue) from source (red) to receiver (green). Centre column shows the path density and right-hand column the azimuthal coverage for Rayleigh and Love waves at the respective periods.

The most pronounced contrasts are at shorter periods, between the high velocities along the mid-Atlantic ridge and the low velocities covering large parts of the Norwegian Sea and North Sea where large sedimentary covers are well documented from hydrocarbon exploration. At longer periods (80 s Rayleigh), the southern limit of the (faster) East European Craton becomes significantly sharper with contrasting (negative) anomalies imaged to the west. We also observe a significant geometrical change of this contrast as compared to the reference, especially in the central part of our study region.

3.1 Resolution

The path density (Fig. 3) is such that the best resolution is obtained over large parts of Central Europe and southwestern Scandinavia. The North Atlantic west and north of the British Isles is resolved with an estimated lateral resolution length of about 250 km at 40 s periods and about 320 km at 80 s for Rayleigh waves. Due to the reduced number of observations for Love waves, especially at longer periods, the resolution is a bit weaker for Love waves west of the British Isles but otherwise similar to the resolution of Rayleigh waves.

From the path density maps, a directional maximum of path density between Iceland and Central Europe crossing the North Sea is indicated. This results from the large number of observations from the temporary HOTSPOT deployment, with many subparallel paths from earthquakes in the central and eastern Mediterranean, combined with the sparseness of data in the rest of the mid-Atlantic. The reduced azimuthal coverage in a northwest direction across the North Sea, due to an overweight of paths in a given direction, nicely illustrates this (e.g. Rayleigh and Love azimuthal coverage at 25 s in Fig. 3).

To ensure that this data distribution does not introduce biases in the tomographic maps, we ran an inversion of a subset of our data, excluding all recordings from the HOTSPOT deployment as well as all data from the NORSAR array in Southern Norway. The path and azimuthal coverage of this reduced data set is presented in Fig. 7. At, for example, Rayleigh 25 s, the total number of observations is reduced by more than 30 per cent whereas at longer periods the

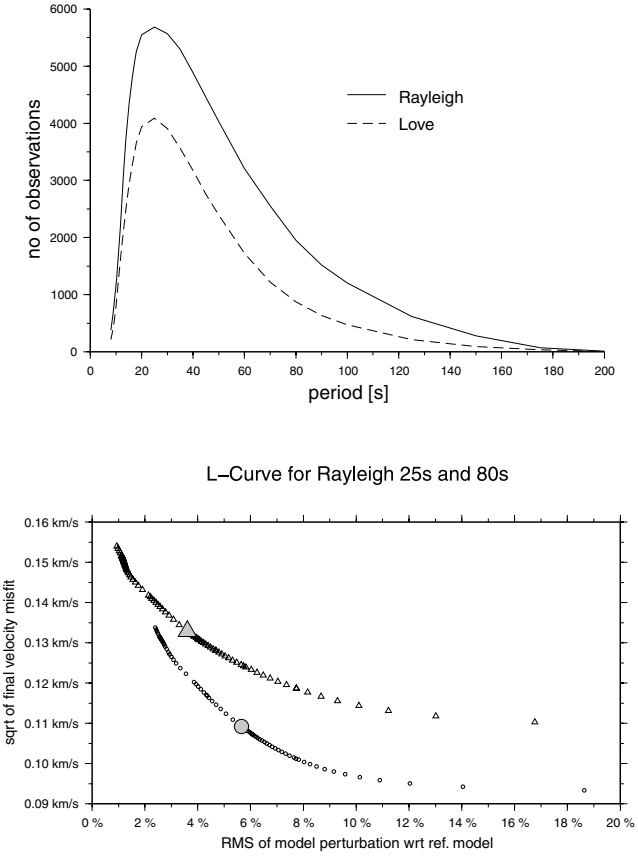

Figure 4. (Top) Number of measurements as a function of period for Rayleigh (solid) and Love (dashed) waves. (Bottom) Trade-off plot of tested parameter combinations for 2-D inversion of Rayleigh waves at 25 s (circles) and 80 s (triangles). The large, grey-filled circle and triangle marks the chosen set of parameters for Rayleigh waves at 25 and 80 s, respectively.

reduction in amount of data is less important (about 15 per cent reduction at Rayleigh 80 s). While the path density especially in the North Atlantic decreases, we observe, on the contrary, a better azimuthal coverage in the North Sea and the North Atlantic and only minor deviations from the azimuthal coverage of the full data set elsewhere. The group velocity maps resulting from the inversion of the data subset differ also only slightly from the ones derived from the full data set. Minor changes are observed in amplitudes but almost no changes in geometries. We conclude that using the full data set does not introduce a directional bias in the model, and that this is in particular true between Iceland and Central Europe.

Further resolution constraints are presented in Fig. 8 which shows synthetic reconstruction tests with different synthetic input models. We created synthetic, spaced checkerboard structures with alternating ± 5 per cent perturbation in group velocity, with lateral extensions of $6^\circ \times 3^\circ$ (top row) and $10^\circ \times 5^\circ$ (middle row). As a third test (bottom row), we stripped the inversion result from the 80 s Rayleigh inversion to a ± 5 per cent model where all amplitudes larger than $+5$ per cent were set to $+5$ per cent, all amplitudes lower than -5 per cent were set to -5 per cent and the remaining amplitudes were set to 0 per cent perturbation. By tracing Gaussian rays through these models, we generate synthetic data with the same source–receiver distributions as in the real data and invert them consequently without (left-hand column) and with (right-hand column) added random Gaussian noise with a standard deviation of $\sigma = 0.05$ km s^{-1}. The same set of regularization parameters as for the real data inversion was applied in these tests.

While the no-noise inversion nicely reflect the influence of the data coverage, with almost perfect reconstruction on mainland Europe and slight smearing in the North Atlantic (25 s Rayleigh, top left-hand side), addition of noise to the data degrades the results. The general patterns are still recoverable, but we observe minor changes and shifts in geometry and amplitudes of the original anomalies. The artefacts, related to the lack of resolution show, however, significantly smaller amplitudes in our reconstruction tests than the structural anomalies, even with added noise. We thus conclude that the major structural features in the model, that is, the ones with sufficiently large amplitudes, prevail the artefacts that result from data uncertainties.

4 DEPTH INVERSION FOR SHEAR WAVE SPEED

For the inversion of the group velocity maps for 3-D shear wave velocity structure, we employ a different approach than Levshin *et al.* (2007), namely a linear inversion scheme following the method described by Maupin & Cara (1992) which we adapt here for inversion of group velocities.

The group velocity data were locally inverted in terms of continuous variations with depth of the elastic parameters, using the method for linear inversion of Tarantola & Valette (1982). Group, phase velocities and partial derivatives in different initial models (as detailed below) were calculated using the software of Saito (1988), and the partial derivatives of the group velocities with respect to elastic parameters were obtained by simple numerical differentiation of the classical phase velocity partial derivatives (Rodi *et al.* 1975). Since we are inverting for continuous depth variations, the smoothness of the model variations with depth has to be controlled explicitly by assuming some *a priori* correlation between the variations of a parameter at different depths. This control is achieved by a non-diagonal *a priori* covariance matrix. The inversion is then dependent on this *a priori* information and not on the discretization of the model with depth. We used Gaussian *a priori* correlation functions (as in Lévêque *et al.* 1991) with a correlation length of 20 km in all layers. The correlation was suppressed between points lying in different layers, for example, between crustal and mantle points, and normalized close to interfaces to compensate for the decrease in total integral value caused by the decoupling across the layer interface. This procedure was thoroughly checked on synthetic examples and proved to stabilize the inversion especially at shallow sub-Moho levels.

We inverted for variations in the two parameters best resolved by surface waves: the *S*-wave velocity V_{SV} and the parameter $\xi = (V_{SH}/V_{SV})^2 = \frac{N}{L}$ (in the common Love notation of elastic parameters in transverse isotropic media, e.g. Saito 1988). For both parameters, we assign an *a priori* standard deviation of 0.2 (in km s^{-1} in V_{SV} and unitless in ξ). We neglect the contribution of changes in V_P and density to surface wave group velocities.

In the period range we used, group velocities are almost not sensitive to mantle *P*-wave velocities (Fig. 9). Rayleigh waves at longer periods are sensitive to mean crustal V_P and at shorter periods to upper crustal V_P. Taking into account that the reference crustal models we apply give better constraints on *P*-wave velocities than we would ever achieve from inversion of Rayleigh wave observations, we decided to perturb V_P neither directly nor through coupling to V_S during the inversion. We also refrained from

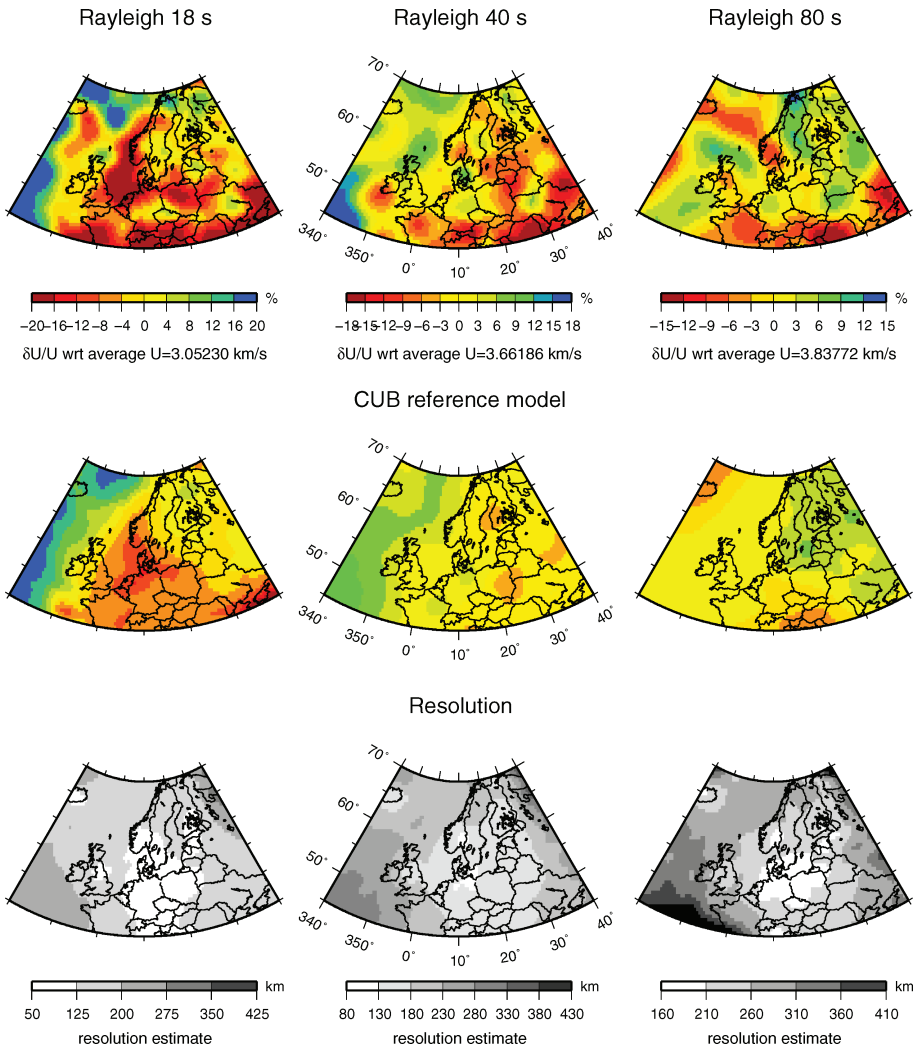

Figure 5. 2-D group velocity maps for Rayleigh waves at periods 18, 40 and 80 s (columns). Top row shows inversion result, middle row reference model and bottom row the resolution estimate.

inverting for density. Partial derivatives of group velocities with respect to density are overall larger than those with respect to V_P (Fig. 9) but have a more oscillatory behaviour which makes depth inversion of Love and Rayleigh wave velocities with respect to density unstable (Cara *et al.* 1984). Since the scaling factor between relative density and *S*-wave velocity anomalies in the mantle is uncertain and may be as low as 0.05 (Deschamps *et al.* 2001), we expect that coupling of density and *S*-wave velocity variations would not affect our *S*-wave model significantly.

In awareness of the trade-off between velocity and interface depth on group velocity partial derivatives, we also choose not to invert for interface depths. Instead we evaluate the impact of the initial model, particularly crustal thickness and structure on the inverted one by testing several initials models of increasing complexity.

4.1 Initial models

Covering a region that extends from the mid-Atlantic ridge in the west to old cratonic provinces in the east, the assumption of a pure 1-D reference profile like PREM (Dziewonski & Anderson 1981) for the entire region will certainly be insufficient. We apply it nonetheless to evaluate the impact of a crust that differs significantly from reality at a vast number of points in our study region. To account for 3-D crustal variations, we set up a model consisting of a 3-D crust and a 1-D mantle profile. Taking the crustal parameters from CRUST2.0 (Bassin *et al.* 2000), we merge the *P*- and *S*-wave velocity from sub-Moho (as of CRUST2.0) with ak135 (Kennett *et al.* 1995) at 120 km depth through spline interpolation. In addition, we removed the 1 promille discontinuity in ak135 at 220 km depth. The resulting reference model of *P*- and *S*-wave velocities will be referred to as CR2AK.

Very recently, a compilation of regional crustal models in Europe has been published (EUCRUST07, Tesauro *et al.* 2008) which includes much more detailed crustal geometries. A comparison of Moho depths (which will turn out to be the most important constraint for our inversion) from a smoothed version of EUCRUST07 (on a $0.5^\circ \times 0.5^\circ$ grid) and CRUST2.0 (Fig. 10) reveals that there are partly differences of more than 15 km between the two models, especially in the North Atlantic. We hence construct another reference model on the basis of EUCRUST07. Since the latter only contains V_P in the crystalline crust, we assign standard values of $V_P = 3.6\ \mathrm{km\,s^{-1}}$ and $V_S = 2.4\ \mathrm{km\,s^{-1}}$ to sediments, convert V_P to V_S in the crystalline crust as $V_P = 1.75 \times V_S$ and apply ak135 (*P*- and *S*-wave velocity) directly at sub-Moho depth. We refer to this reference as EUCAK.

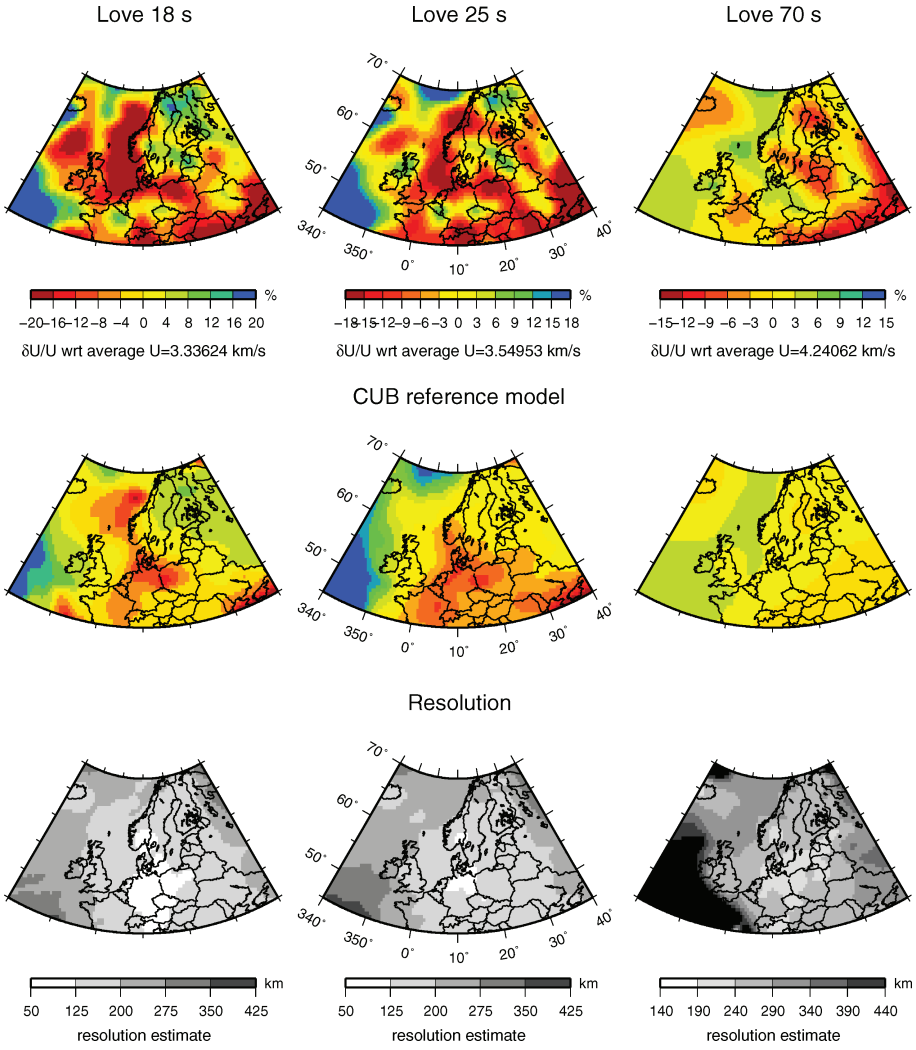

Figure 6. Similar as Fig. 5 but for Love waves at periods 18, 25 and 70 s.

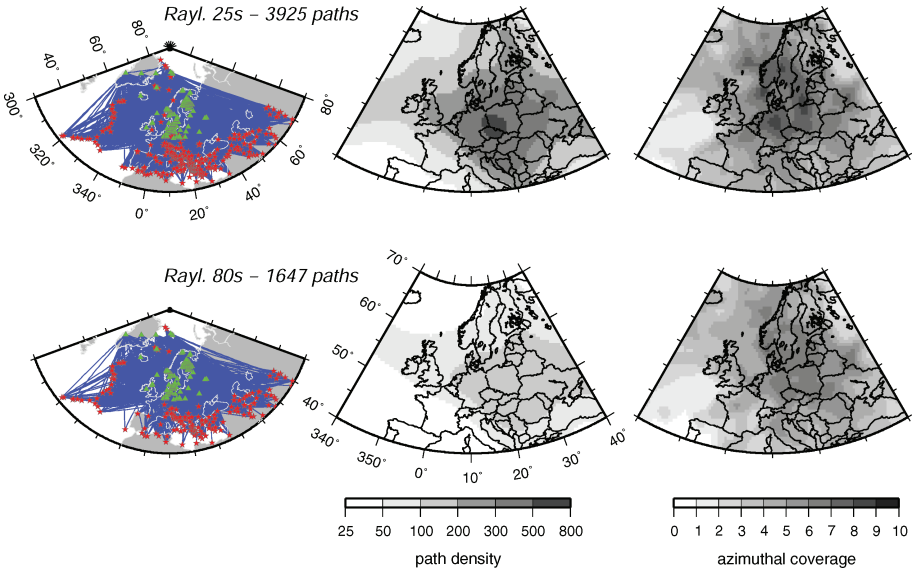

Figure 7. Data coverage, path density and azimuthal coverage for subset of data that excludes recordings from the HOTSPOT network on Iceland and from NORSAR array in Southern Norway. See caption in Fig. 3.

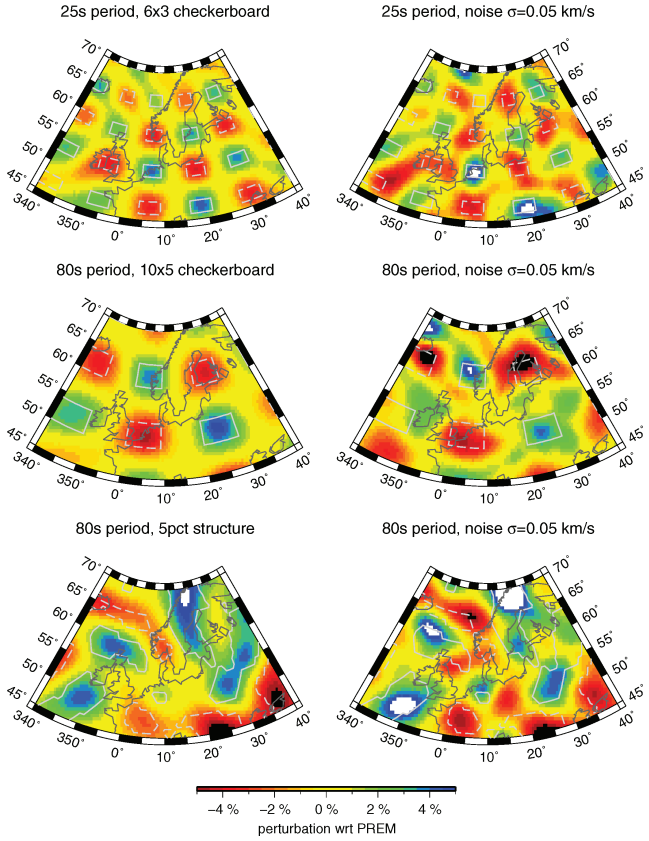

Figure 8. Synthetic reconstruction tests. Left- and right-hand columns show inversions of synthetic data without and with added random Gaussian noise ($\sigma = 0.05$ km s^{-1}). Spaced checkerboards with $6^\circ \times 3^\circ$ boxes for 25 s Rayleigh waves (top row) and $10^\circ \times 5^\circ$ boxes for 80 s Rayleigh waves (middle row) as well as a synthetic structure test for Rayleigh waves at 80 s (bottom row) are presented. Solid and dashed lines mark positive and negative 5 per cent perturbation contours of input models, respectively.

As a last approach, we applied a fully 3-D model of shear wave velocity as a reference for our inversion. We chose the global model derived by N. Shapiro on a $2^\circ \times 2^\circ$ degree grid with a Monte-Carlo inversion (Shapiro & Ritzwoller 2002). This model will be referred to as CUB20 in the following.

4.2 Isotropic inversion

We performed first a joint inversion of the Love and Rayleigh wave group velocities with respect to isotropic *S*-wave velocity. Fig. 11 shows the misfit of the data before (left-hand panel) and after linear, isotropic inversion (centre panel) at two periods (30 and 80 s) for both Rayleigh and Love waves (with EUCAK as the reference). The rms reduction in the entire study region after isotropic inversion is well above 55 per cent for a large range of periods.

Comparing the remaining misfit for Rayleigh and Love waves after isotropic inversion, we observe a clear difference in the average misfit. Whereas the final residuals for Rayleigh waves remain mostly negative, the Love wave residuals are in general positive, especially at longer periods. This is an indication that the inversion is unable to explain simultaneously Love and Rayleigh wave data with an isotropic model. This Love–Rayleigh discrepancy is commonly explained by the presence of transverse isotropy, where the *SV* waves which form the Rayleigh waves have a different velocity than the *SH* waves that form the Love waves (see Maupin & Park

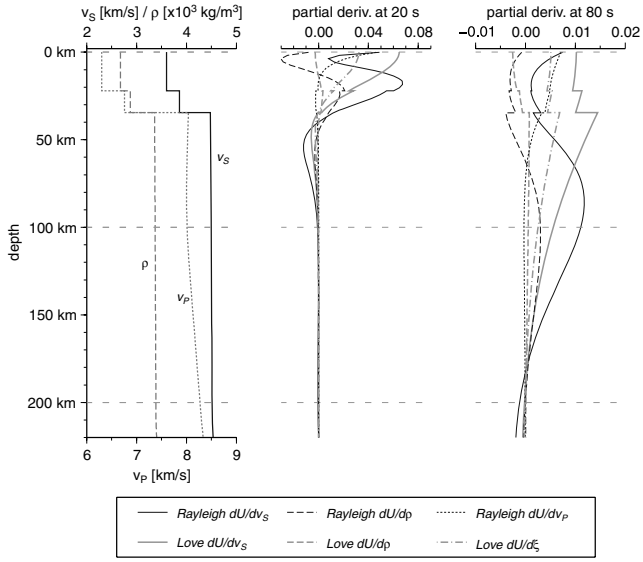

Figure 9. Partial derivatives of Love and Rayleigh group velocities at 20 s (centre) and 80 s (right-hand side) period calculated in reference model EUCAK (see Section 4.1) at 60°N/10°E (left-hand side).

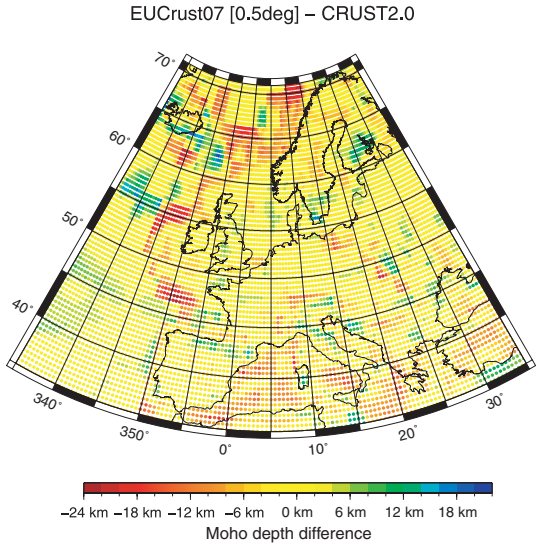

Figure 10. Difference in Moho depth between EUCRUST07 (Tesauro *et al.* 2008) (smoothed on a $0.5^\circ \times 0.5^\circ$ grid) and CRUST2.0 (Bassin *et al.* 2000).

2007, for a recent review). To take this observation into account, we also invert for the anisotropy parameter ξ. The ultimately remaining misfits after anisotropic inversion are shown in the right-hand panels of Fig. 11 and yield that the misfit is reduced approximately to half of the misfit after isotropic inversion. The total rms reduction in the entire study region is close to 80 per cent at shorter periods and well above 60 per cent at longer periods.

4.3 Anisotropic inversion and effect of crustal structure

In the present study, we do not analyse the azimuthal variation of Love and Rayleigh group velocity but their average with respect to azimuth. The data are therefore only sensitive to the azimuthal average of the anisotropic parameters. The Love and Rayleigh wave 2-D group velocity maps were inverted simultaneously for the two

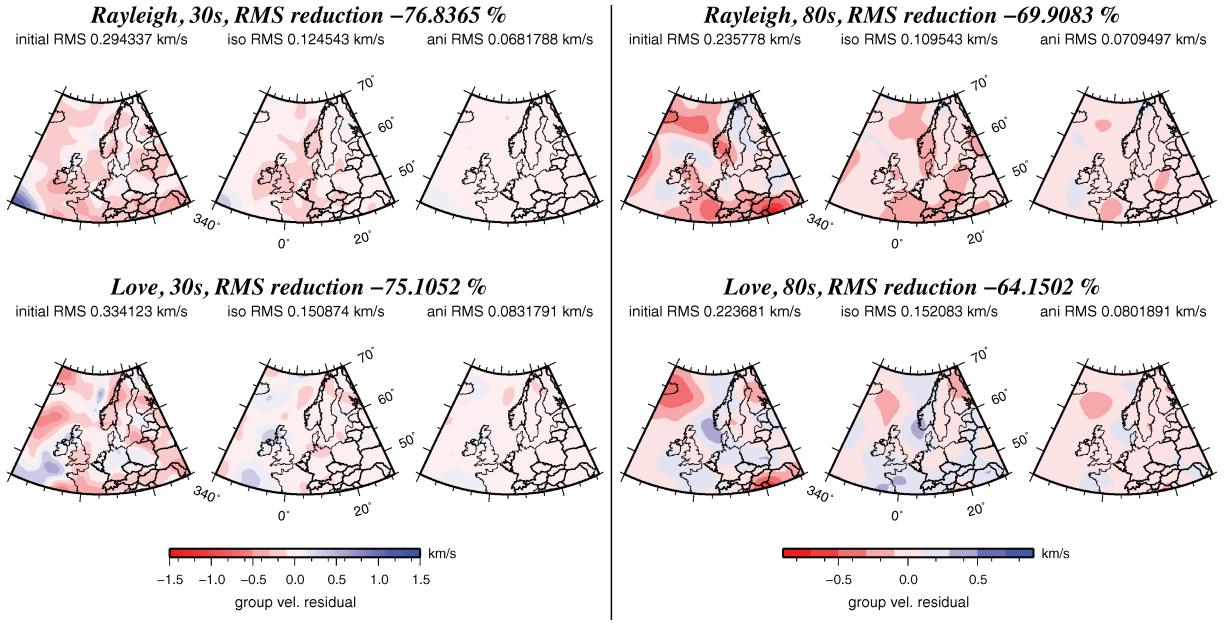

Figure 11. Initial and final data misfit maps before and after linear, isotropic and anisotropic inversion at 30 s (left-hand panel) and 80 s (right-hand panel) period. Top row shows Rayleigh wave misfit before (left-hand side), after isotropic (centre) and after anisotropic (right-hand side) inversion, bottom row similarly for Love waves.

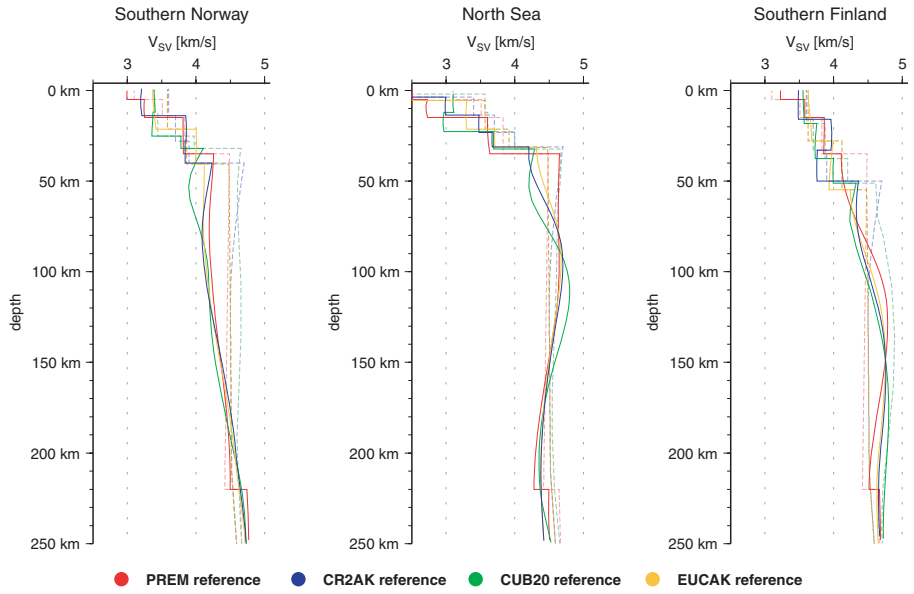

Figure 12. Linear inversion of inverted group velocities at three different locations: Southern Norway (left-hand side), North Sea (centre), Southern Finland (right-hand side). Each plot shows the reference profile (dashed) and the inversion result (solid) for four different reference models: PREM (red), CR2AK (blue), CUB20 (green) and EUCAK (orange).

transverse isotropic parameters which are best resolved by azimuthally averaged surface wave velocities: V_{SV}, the azimuthally averaged velocity of horizontally propagating SV waves, and the anisotropic parameter $\xi = (V_{SH}/V_{SV})^2$ measuring the difference between the azimuthally averaged velocity of horizontally propagating SH and SV waves.

We perform linear inversions on the respective reference model grids (1° × 1° degree grid with PREM and EUCAK and 2° × 2° degree grid with CR2AK and CUB20) in the frame 45°– 70°N/20°W–30°E and find very consistent results for depths greater than 70 km in all resulting models (each based on a different reference). A comparison of the results is given in Fig. 12 which displays all four reference (dashed lines) and resulting (solid lines) profiles at three different locations, in Southern Norway (left-hand side, 60.5°N/9.5°E), the North Sea (middle, 58.5°N/3.5°E) and Southern Finland (right-hand side, 62.5°N/25.5°E).

Although the crustal models, in particular Moho depths vary between the respective reference models locally by more than 15 km (e.g. Southern Finland, PREM Moho at 35 km, CUB20 Moho at 51.2 km), the inversion results at mantle depths beneath around 70 km are consistent, irrespective of the reference model. At shallower depths however, the accuracy of the crust shows its

importance. In the North Sea example (Fig. 12 middle), CRUST2.0, EUCAK and CUB20 Moho depths are very similar (31.2, 30.2 and 32.3 km, respectively) and consequently is the velocity distribution at sub-Moho depths. Although PREM Moho depth differs only slightly from the other models at this location, the resulting velocity beneath Moho is significantly higher than in the other cases (at 45 km the PREM-derived model is 7 per cent faster than the EUCAK-derived, whereas the CUB20- and CR2AK-derived are around 3 and 1 per cent slower, respectively). In Southern Finland, on the contrary, the profiles are more consistent at shallow mantle depths, although the Moho depth of EUCAK (58.8 km) differs quite significantly from the other local models (50.0 and 51.2 km in CR2AK and CUB20, respectively), and even more from PREM.

Comparing the inversion results within the crust, no consistencies between the respective reference models can be observed. Although the internal layering is in some cases very similar, for example, in the North Sea, the resulting velocities show large differences between the respective models. We interpret this as compensational effects to fit the data into an untrue crust framed by fixed interfaces.

Although Fig. 12 compares inversion results after anisotropic inversion, we observe very similar relative variations in V_S upon isotropic inversion. We interpret that as an indication the relative differences observed here between the models are not a result of a trade-off between V_{SV} and ξ in the inversion. The crustal structure has, of course, also an influence on the results of the inversion in ξ. We observe variations in $\sqrt{\xi}$ of ± 0.05 in the mantle when changing the crustal model which means that we have, in general, a robust information on the sign of $\sqrt{\xi} - 1$ but that its amplitude should be interpreted with caution.

The influence of the crustal model on group velocities is apparently a more non-linear phenomenon than its influence on phase velocities, and the tests discussed above show the complexity of the trade-off between crustal and sub-Moho structures. They also quantify the limitations of our tomographic sub-Moho models in the absence of better constraints on crustal structure.

From these observations, it becomes clear that our discussion has to focus on mantle depths. Inclusion of sub-Moho features is reasonable as the trends persist, but care has to be taken on the absolute values for depths shallower than ~70 km. Since the resulting models of shear wave speed at mantle depths are consistent irrespective of the reference model, we will, in the following, present and discuss the model derived from reference model EUCAK in more detail.

4.4 Three-dimensional model

The V_{SV} velocity model reveals unprecedented details of regional structures including some intriguing aspects. Fig. 13 shows four depth maps of the V_{SV} model in direct comparison with the global 3-D model of isotropic shear wave speed CUB2.0, at corresponding depths (Shapiro & Ritzwoller 2002) to illustrate the improvement.

Taking into account that the southeastern and southwestern corners of the maps are the areas with the least resolution, we find that our new model to a large extent preserves the large-scale features of the east–west transition through tectonic domains, especially at the largest depths. Extended regions of low velocities are clearly related to the mid-Atlantic ridge system and the Iceland plume domain whereas the eastern parts of the models are dominated by high-velocity anomalies related to the East European Craton. It has to be noted though that this high-velocity anomaly has a significantly different geometry in southwestern Scandinavia compared to the CUB2.0 model.

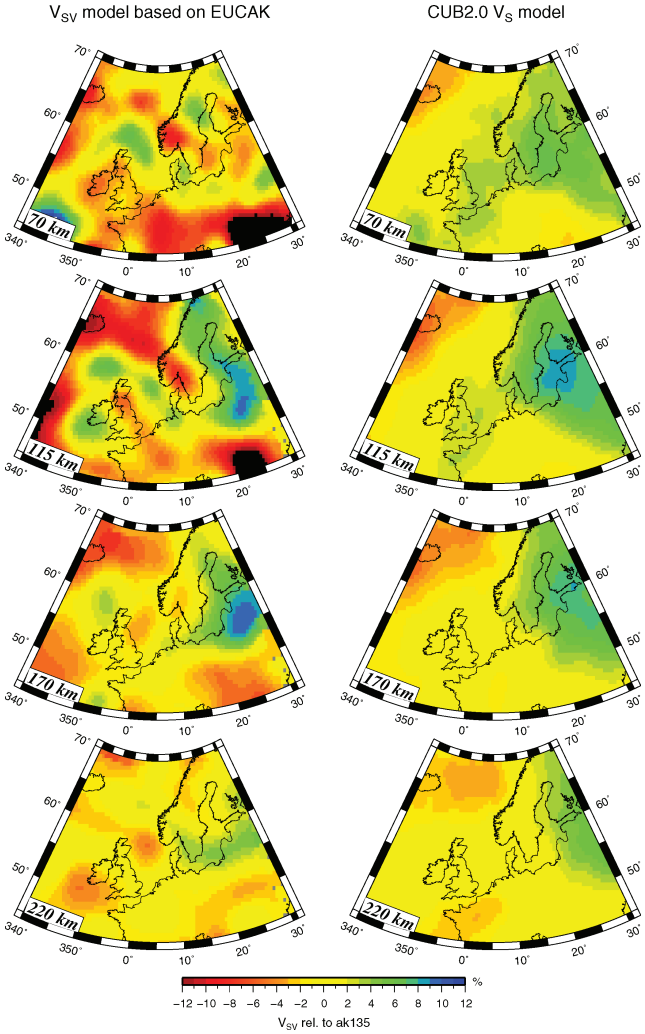

Figure 13. V_{SV} model based on EUCAK reference at 70, 115, 170 and 220 km depth (left-hand column) and the 3-D model CUB20 (Shapiro & Ritzwoller 2002) at corresponding depths (right-hand column) for comparison.

Superimposed on the first-order east–west gradient, we can now resolve bands of rather large positive and negative anomalies in a northwest–southeast trend. This is especially well-marked at 115 km depth. Of particular interest is the southeast directed low-velocity anomaly stretching from Iceland and the Norwegian Sea to southwestern Scandinavia. It can be clearly traced from 90 to 140 km depth but might be even shallower.

Fig. 14 presents map views of the resulting V_{SV} model (left-hand side) and the distribution of $\sqrt{\xi} - 1$ (right-hand side, given in percent) at three depths complementary to those presented in Fig. 13. The anisotropy appears also rather strong, with amplitudes reaching at least 10 per cent.

In general, the patterns of anisotropy reveal geometries that are not related to first-order tectonic features. The values of $\sqrt{\xi} - 1$ are dominantly positive at shallow depth, in accordance with many other studies of the same kind and in particular in accordance with values in PREM (Dziewonski & Anderson 1981). At shallow depths, anisotropy appears to be highest in the oceanic domains to the west. Negative variations are observed in the Gulf of Bothnia in the vicinity of the region where the maximum rate of uplift related to

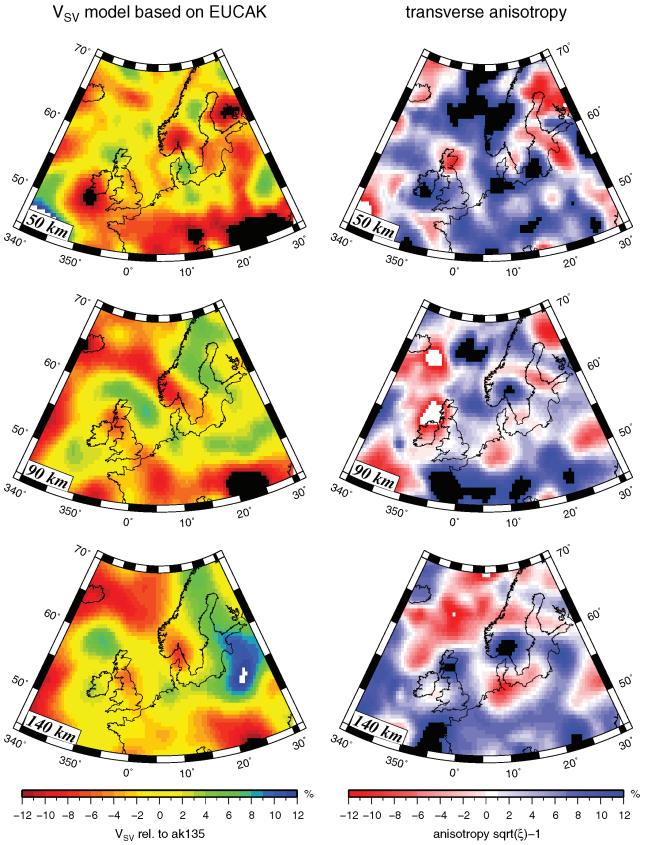

Figure 14. Preferred V_{SV} model based on EUCAK reference at 50, 90 and 140 km depth (left-hand column) and transverse anisotropy ($\sqrt{\xi} - 1$) (right-hand column). The presentation of the V_{SV} model is complementary to Fig. 13.

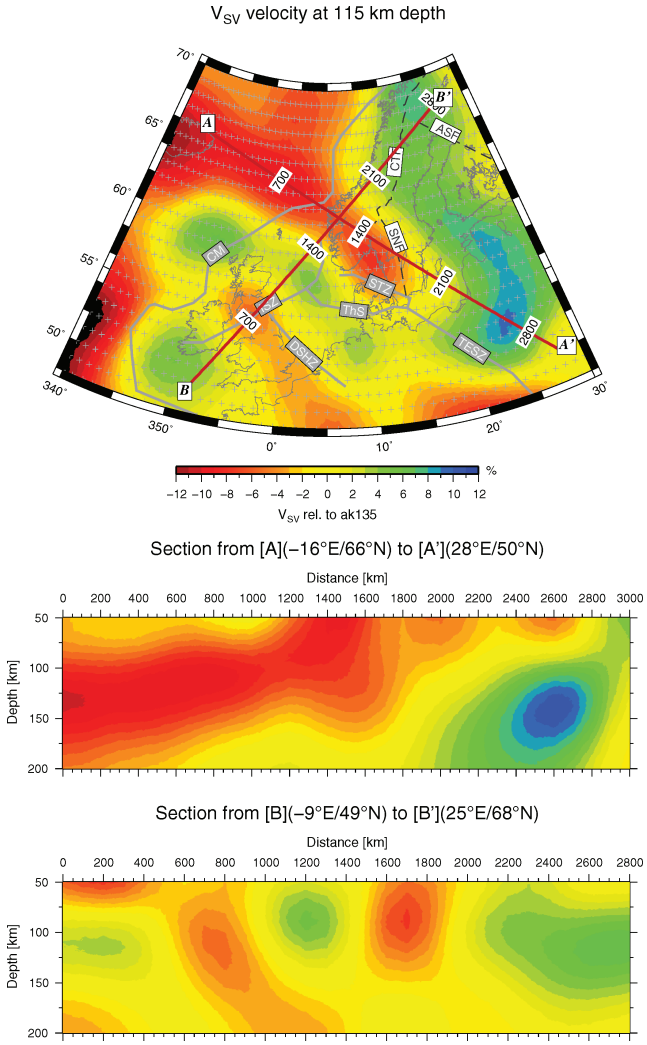

Figure 15. Top: Map view at 115 km depth through the V_{SV} model based on EUCAK. Dark red lines indicate locations of cross-sections A–A′ and B–B′. Annotated grey lines show schematically the continental margin and major crustal boundaries after Winchester (2002). Annotations as in Fig. 1. Light grey crosses mark points of nominal resolution. Bottom: Cross-sections A–A′ and B–B′.

postglacial rebound is observed (Johansson *et al.* 2002). At 90 km depth, the amplitude of the anisotropy is slightly reduced, with several regions of negative anomalies, especially under the northern British Isles. Maps of V_{SH} can be obtained by combination of the V_{SV} and $\sqrt{\xi} - 1$ maps. In some locations, like in the North Sea or in Ireland, the anomalies in V_{SH} are amplified (compared to V_{SV} and with respect to the reference), whereas they are attenuated in other regions, in particular in Southern Norway. The anisotropy at 140 km depth is not as well constrained as the V_{SV} model due to the shallower sensitivity of Love compared to Rayleigh waves and we will hence refrain from going into the details of the anisotropy map at that depth.

5 DISCUSSION

The amplitudes of the heterogeneities in our model, both in V_{SV} and in anisotropy are in excess of ±10 per cent. Although this level of heterogeneity is commonly considered to be high for a mantle model, similar levels of heterogeneities have been found in comparable regional studies (e.g. Lévêque *et al.* 1998 for the Indian Ocean, Debayle & Kennett 2000 for Australia, Marone *et al.* 2004a,b for the Mediterranean region or Feng *et al.* 2004, 2007 for South America). We have made a series of tests, as detailed in the previous section, to ensure that the location and amplitude level of the heterogeneities is not a result of underdamping in the inversion. The main uncertainty comes from the biases which can be introduced in the upper part of the mantle due to inaccuracies in crustal structure, primarily Moho depth. This non-linear effect, that is, dependence of velocities and interface depth is in other studies often tackled by search algorithms like Monte-Carlo (e.g. Shapiro & Ritzwoller 2002) or neighbourhood algorithm (e.g. Yao *et al.* 2008). Since our focus is on upper-mantle structure rather than resolving crustal features, we chose to apply well-constrained regional crustal models derived mostly from active seismics, to stabilize the inversion at depth. Our tests show that large variations of crustal structure affect the models significantly at shallow mantle depths, but that the results in V_{SV} at 70 km depth and below are stable. We will therefore focus our discussion of the V_{SV} model on depths beneath 70 km and refer in this mainly to Fig. 15, but also to Figs 13 and 14. We will first compare our model to published results and then discuss the trends in the model in light of the tectonic history of the area.

Comparing our model with the *P*-wave tomography model by Bijwaard *et al.* (1998) and the *S*-wave model by Marquering & Snieder (1996) based on *S* and Rayleigh waves (regional plots of these models are also presented in Goes *et al.* 2000), we find a better correlation to the *P*-wave model (at 100 km depth) than to the

S-wave model. The *P*-wave tomography clearly images the continuous low-velocity regime between Iceland and Southern Scandinavia, slightly deeper than in our model but also with less vertical confidence in the uppermost mantle (as in Plate 5 of Bijwaard *et al.* 1998). This feature is confirmed by the recent *P*-wave model by Amaru (2007) who employ a larger data set than Bijwaard *et al.* (1998).

On the contrary, the *S*-wave model by Marquering & Snieder (1996) is dominated by low velocities beneath the North Sea and North–Central Europe; however, the relative variations beneath the North Sea and the British Isles are consistent with our model. Beneath the British Isles, both models are slower as compared to the North Sea and also north and east of the Isles. In fact, even the high-velocity pattern imaged in our model west of Ireland, which is definitely at the margin of our well-resolved model area, is consistent with the model by Marquering & Snieder (1996) and also the surface wave-derived V_{SV} model by Pilidou *et al.* (2004, 2005).

The latter model (Pilidou *et al.* 2004, 2005) correlates in the entire study region well with our results. Both the extension of low velocities from Iceland beneath the Norwegian Sea and the high velocities around the British Isles are consistently imaged. But also other anomalies, for example, the low velocities contrasting the fast East European Platform at ∼45°N/20°E and 100–150 km depth are in agreement. The major inconsistency between our and *Pilidou et al.*'s model is the low-velocity channel reaching from Iceland and the Norwegian Sea beneath southwestern Scandinavia, the most intriguing element of our model. Although low velocities are indicated in Pilidou *et al.*'s model at 150 km and deeper beneath large parts of the North Sea including Southern Norway and Denmark, no connection to the Iceland–mid-Atlantic low-velocity regime is seen there. We attribute that to their correlation length of 400 km, which corresponds to about the minimum width of the channel we image.

In our model, this feature is well above the resolution limit and thus stable. Section A–A′ in Fig. 15 shows the continuous structure in a cross-section from Iceland across southwestern Scandinavia and into the East European Platform. The negative perturbation beneath Norway is continuously around −10 per cent relative to ak135 between 70 and 115 km depth, and the anomaly in the 'channel' is continuously below −6 per cent between 80 and 130 km depth. From our resolution analysis, we would expect significantly smaller amplitudes if this pattern was an artefact from lateral smearing. The indicated shallowing of the anomaly, from 70 km upward, beneath Southern Norway remains an open issue, without further constraints on crustal parameters.

The extension of the North Atlantic low-velocity regime below Southern Norway is intriguing as it coincides with the location of the southern dome of the Scandes mountain range. This region has been submitted to significant uplift during Neogene and has a present maximum elevation of 2469 m. Different scenarios have been proposed but the origin of the uplift is still unknown (Clift *et al.* 1998; Japsen & Chalmers 2000; Lundin & Dore 2002). It seems clear, however, that some mantle processes must be at play. From analysis of gravity data, Ebbing & Olesen (2005) infer that a modified diapirism model linking to the Iceland plume could explain the observed uplift in Southern Norway. Our tomographic 3-D structure would be in support of such a scenario.

The extension of this low-velocity region beneath Southern Sweden is, however, somewhat contradictory to the general observation of an increase in lithospheric thickness northeast of the STZ. Both surface and body wave studies (Cotte & Pedersen 2002; Shomali *et al.* 2006, respectively) show a contrast in *S*-wave velocity of the opposite sign than in our model. We will not argue that our model can compete in terms of lateral resolution with these results, but the drop in V_{SV} perturbation at around 1800 km along section A–A′ in our model might be an indication to a change in upper-mantle structure along the profile. It coincides approximately with the Svecofennian (early Proterozoic)—Sveconorwegian (middle-late Proterozoic) boundary (SNF, e.g. Windley 1992). With respect to the synthetic tests presented earlier, we also have to consider the possibility that our imaged geometries are slightly perturbed due to uncertainties in the data. This discrepancy will thus require close attention in further studies.

Further north, the Scandes range has a second centre of high topography. Ebbing & Olesen (2005) noted differences between the lithospheric properties of the southern and northern mountain ranges from analysis of gravity data. They suggest that uplift originated mainly as a rift-shoulder in the north and does not require, as in the south, the involvement of deep mantle processes. Again, our model would support their suggestions in terms of present upper-mantle structure as we do not image any significant negative mantle anomaly in the north.

Remarkably, the eastern bound of the low-velocity region in the Norwegian Sea aligns nicely with the continental margin offshore Central Norway. The same alignment of lithospheric geometries with the continental margin can be observed west of Ireland whereas the respective geometries are somewhat perpendicular to each other north of the British Isles.

There is no clear imprint in our model of the ISZ, the boundary between Laurentia and Avalonia across the British Isles. This correlates with findings by Arrowsmith *et al.* (2005) and Landes *et al.* (2007) who could not observe a mantle signature of the suture beneath Britain and Ireland, respectively. The low-velocity maximum imaged at 90 and 115 km depth beneath northwestern Britain and the Irish Sea is in good agreement with the model by Arrowsmith *et al.* (2005).

The North Sea appears as a region of high velocities, bordered to the southwest by the Dowsing-South Hewett Fault Zone (DSHZ) and to the northeast by the STZ. Winchester (2002) distinguishes 'Far Eastern Avalonia', covering most of the North Sea northeast of the DSHZ from the main Avalonia plate. We image a transition that would support his hypothesis that these two units of the Avalonian plate are two different lithospheric blocks.

The TESZ is imaged as a sharp contrast in Eastern Europe, but the geometry of the craton is strongly perturbed as compared to a global reference model (Fig. 13). Especially the transition across the STZ in Southern Scandinavia is apparently inconsistent with the results from the TOR project as discussed earlier.

Pegrum (1984) noted the possiblity for the STZ (as the northwesternmost element of the TESZ) to extend into the Norwegian North Sea, and possibly even further northwest until the Scottish shelf. We can note that this line, which aligns with the Iceland-Faroer volcanic ridge, also aligns with the southern bound of our observed low-velocity channel in the upper mantle.

In Finland, the large-scale transition from the Proterozoic Svecofennian to the Archean Kola-Karelian orogen (ASF) is nicely imaged in our model between 115 and 170 km depth, in accordance with the surface wave study of SVEKALAPKO data by Bruneton *et al.* (2004).

The continuation of our model to the north is also very consistent with the Barents Sea model by Levshin *et al.* (2007) as both image at around 100–150 km depth—the transition from low velocities associated with the close by mid-Atlantic ridge system to higher values in the continental region.

Given the sensitivity of Love waves in the frequency range of our data, we restrict our discussion in terms of anisotropy to 50 and 90 km depths. The strongest anomalies at 90 km depth in Central Europe correlate nicely with similar anomalies found by Marone *et al.* (2004b). At 50 km depth, positive and large values of anisotropy cover almost the entire Northeast Atlantic, eventually extending underneath the continent in Southern and Central Norway. Positive $\sqrt{\xi} - 1$ values are common in oceanic regions at that depth (e.g. Nishimura & Forsyth 1989). Two negative anomalies are located below Ireland (90 km depth) and the northern part of the Bothnian Bay (50 km depth).

The classical interpretation of the ξ parameter in the mantle is in terms of orientation of olivine crystals by mantle deformation. In this context, negative values of $\sqrt{\xi} - 1$ are associated with vertical extension, whereas positive values are associated with horizontal extension. Purely horizontally oriented olivine yields values of $\sqrt{\xi} - 1$ of about 0.11 (see e.g. Pedersen *et al.* 2006). Considering the uncertainty of about 0.05, our maximum values of anisotropy are not incompatible with an interpretation in terms of orientation of olivine but are at the limit of what can be expected. Although the interpretation in terms of olivine orientation is well accepted at large scale, large values of $\sqrt{\xi} - 1$ at smaller (regional) scale as found in this and several similar studies in other regions, may originate partly from other yet unknown features.

Without pushing the interpretation of the anisotropy found in this study too far, we note that the negative anomaly around the Bothnian Bay may be seen in the context of the maximum rate of uplift related to postglacial rebound in the same region (Johansson *et al.* 2002). This might indicate that the rebound is associated not only with deep asthenospheric flow but also with a deformation of the above lying lithosphere. A mean positive value of about 5 per cent has been found in the lithosphere beneath Finland (Pedersen *et al.* 2006), a region where we image a transition from negative values in the north to positive values in the south.

Along the low-velocity anomaly imaged in V_{SV} that extends from Iceland to Southern Norway, we would expect a positive anomaly in anisotropy if the heterogeneity were associated with simple horizontal flow. Apparently, we do not observe any such simple pattern of anisotropy and must hence expect that the origin of this structure is of more complex nature.

6 CONCLUSIONS

We collected regional surface wave observations from international and regional data archives to measure group velocities for both Love and Rayleigh surface waves. Inversion for 2-D maps of group velocity variations was followed by linear inversion for 1-D, transverse isotropic shear wave velocity profiles. These profiles were then assembled to a 3-D model of shear wave velocity and anisotropy in the upper mantle beneath Northern Europe.

Our model is, in general, in good agreement with previous studies but also resolves a number of new features. It highlights a low-velocity channel that connects a low-velocity regime beneath large parts of the North Atlantic to a distinct zone of low velocities in the upper mantle beneath southwestern Scandinavia.The anomaly extends vertically to around 150 km depth beneath Southern Norway. Further constraints on crustal geometries and the geometry of this feature beneath Southern Norway are expected from ongoing data collection, both active and passive.

The presented model allows to trace ancient plate boundaries at lithospheric depths and clearly identifies regions where major crustal trends are opposing upper-mantle geometries as, for example, across the continental margin between the British Isles and Central Norway.

A discussion on the nature of all observed features in our mantle model in a petrological and plate-tectonic context, also the impact of our results on uplift models along the Northeast Atlantic margin, is beyond the scope of this paper, but our new detailed model of the upper mantle beneath Northern Europe may help to improve our understanding of the evolution of topography in this region.

ACKNOWLEDGMENTS

CW was supported by the Norwegian Research Council through a post-doctoral scholarship. Thanks go to J. Schweitzer for providing data from NORSAR and we acknowledge the data centres at University of Bergen, University of Helsinki, the Kola Science Center in Apatity and the Geological Service of Denmark from which we used waveform data. A. Levshin kindly provided global reference maps from the group at Univ. Colorado and software for measuring and inverting group velocities; J.I. Faleide and O. Ritzmann are acknowledged for discussion and comments, as are E. Debayle and anonymous reviewers whose constructive remarks helped to improve an earlier and the present version of this contribution. The 3-D global *S*-wave speed model (Shapiro & Ritzwoller 2002) was retrieved from *http://ciei.colorado.edu/~nshapiro/MODEL/* and the crustal model CRUST2.0 (Bassin *et al.* 2000) from *http://mahi.ucsd.edu/Gabi/rem.html*. Figures were prepared using Generic Mapping Tools (Wessel & Smith 1998).

REFERENCES

Amaru, M.L., 2007. Global travel time tomography with 3-D reference models, *PhD thesis*, Utrecht University, The Netherlands.

Arrowsmith, S.J., Kendall, M., White, N., VanDecar, J.C. & Booth, D.C., 2005. Seismic imaging of a hot upwelling beneath the British Isles, *Geology,* **33**(5), 345–348.

Bannister, S.C., Ruud, B.O. & Husebye, E.S., 1991. Tomographic estimates of sub-Moho seismic velocities in Fennoscandia and structural implications, *Tectonophysics,* **189**(1–4), 37–53.

Barmin, M.P., Ritzwoller, M.H. & Levshin, A.L., 2001. A fast and reliable method for surface wave tomography, *Pure appl. Geophys.,* **158**(8), 1351–1375.

Bassin, C., Laske, G. & Masters, G., 2000. The current limits of resolution for surface wave tomography in north america, *EOS, Trans. Am. geophys. Un.,* **81**(48), F897.

Bijwaard, H., Spakman, W. & Engdahl, E., 1998. Closing the gap between regional and global travel time tomography, *J, geophys. Res.,* **103**, B12(12), 30 055–30 078.

Bruneton, M. *et al.*, 2004. Complex lithospheric structure under the central Baltic Shield from surface wave tomography, *J. geophys. Res.,* **109**, B10303.

Cara, M., Lévêque, J.J. & Maupin, V., 1984. Density-versus-depth models from multimode surface waves, *Geophys. Res. Lett.,* **11**, 633–636.

Clift, P.D., Carter, A. & Hurford, A.J., 1998. The erosional and uplift history of NE Atlantic passive margins: constraints on a passing plume, *J. Geol. Soc.,* **155**(5), 787–800.

Cocks, L.R.M. & Torsvik, T.H., 2005. Baltica from the late Precambrian to mid-Palaeozoic times: the gain and loss of a terrane's identity, *Earth-Sci. Rev.,* **72**(1–2), 39–66.

Cotte, N. & Pedersen, H.A., 2002. Sharp contrast in lithospheric structure across the Sorgenfrei-Tornquist Zone as inferred by Rayleigh wave analysis of TOR1 project data, *Tectonophysics,* **360**(1–4), 75–88.

Debayle, E. & Kennett, B.L.N., 2000. Anisotropy in the Australasian upper mantle from Love and Rayleigh waveform inversion, *Earth planet. Sci. Lett.,* **184**(1), 339–351.

Deschamps, F., Snieder, R. & Trampert, J., 2001. The relative density-to-shear velocity scaling in the uppermost mantle, *Phys. Earth planet. Inter.,* **124**(3–4), 193–212.

Dziewonski, A. & Anderson, D., 1981. Preliminary reference earth model, *Physics Earth planet. Int.,* **25**, 297–356.

Ebbing, J. & Olesen, O., 2005. The Northern and Southern Scandes—structural differences revealed by an analysis of gravity anomalies, the geoid and regional isostasy, *Tectonophysics,* **411**(1–4), 73–87.

Eken, T., Shomali, Z.H., Roberts, R. & Bodvarsson, R., 2007. Upper-mantle structure of the Baltic Shield below the Swedish National Seismological Network (SNSN) resolved by teleseismic tomography, *Geophys. J. Int.,* **169**(2), 617–630.

Engdahl, E., van der Hilst, R. & Buland, R., 1998. Global teleseismic earthquake relocation with improved travel times and procedures for depth determination, *Bull. seism. Soc. Am.,* **88**, 722–743.

England, R., 1995. The seismic signature of the Iapetus Suture beneath the North Sea, *Studia Geophysica et Geodaetica,* **39**(3), 235–240.

Feng, M., Assumpo, M. & Van der Lee, S., 2004. Group-velocity tomography and lithospheric S-velocity structure of the South American continent, *Phys. Earth planet. Int.,* **147**(4), 315–331.

Feng, M., Van der Lee, S. & Assumpo, M., 2007. Upper mantle structure of South America from joint inversion of waveforms and fundamental mode group velocities of Rayleigh waves, *J. geophys. Res.,* **112**, B04312.

Goes, S., Govers, R. & Vacher, P., 2000. Shallow mantle temperatures under Europe from P and S wave tomography, *J. geophys. Res.,* **105**(B5), 11 153–11 169.

Huang, Z., Su, W., Peng, Y. & Zheng, Y., 2003. Rayleigh wave tomography of China and adjacent regions, *J. geophys. Res.,* **108**(B2), 2073.

Husebye, E.S., Hovland, J., Christofferson, A., Åstroöm, K., Slunga, R. & Lund, C.E., 1986. Tomographic mapping of the lithosphere and asthenosphere beneath Southern Scandinavia and adjacent areas, *Tectonophysics,* **128**(3–4), 229–250.

Japsen, P. & Chalmers, J.A., 2000. Neogene uplift and tectonics around the North Atlantic: overview, *Global Planet. Change,* **24**(3–4), 165–173.

Johansson, J. *et al.*, 2002. Continuous GPS measurements of postglacial adjustment in Fennoscandia—1. Geodetic results, *J. geophys. Res.,* **107**(B8), 2157. doi:10.1029/2001JB000400.

Kennett, B., Engdahl, E. & Buland, R., 1995. Constraints on seismic velocities in the Earth from travel times, *Geophys. J. Int.,* **122**, 108–124.

Landes, M., Ritter, J.R.R., O'Reilly, B.M., Readman, P.W. & Do, V.C., 2006. A N-S receiver function profile across the variscides and caledonides in SW Ireland, *Geophys. J. Int.,* **166**(2), 814–824.

Landes, M., Ritter, J. & Readman, P., 2007. Proto-Iceland plume caused thinning of Irish lithosphere, *Earth planet. Sci. Lett.,* **255**(1–2), 32–40.

Lévêque, J.J., Cara, M. & Rouland, D., 1991. Wave-form inversion of surface-wave datatest of a new tool for systematic investigation of upper mantle structures, *Geophys. J. Int.,* **104**(3), 565–581.

Lévêque, J.J., Debayle, E. & Maupin, V., 1998. Anisotropy in the Indian Ocean upper mantle from Rayleigh and Love waveform inversion, *Geophys. J. Int.,* **133**(3), 529–540.

Levshin, A.L., Ritzwoller, M.H. & Resovsky, J.S., 1999. Source effects on surface wave group travel times and group velocity maps, *Phys. Earth planet. Inter.,* **115**(3–4), 293–312.

Levshin, A.L., Schweitzer, J., Weidle, C., Shapiro, N.M. & Ritzwoller, M.H., 2007. Surface wave tomography of the Barents Sea and surrounding regions, *Geophys. J. Int.,* **170**(1), 441–459.

Lundin, E. & Dore, A.G., 2002. Mid-Cenozoic post-breakup deformation in the 'passive' margins bordering the Norwegian-Greenland Sea, *Mar. Petrol.Geol.,* **19**(1), 79–93.

Marone, F., van der Lee, S. & Giardini, D., 2004a. Three-dimensional upper-mantle S-velocity model for the Eurasia-Africa plate boundary region, *Geophys. J. Int.,* **158**(1), 109–130.

Marone, F., van der Lee, S., & Giardini, D., 2004b. Shallow anisotropy in the Mediterranean mantle from surface waves, *Geophys. Res. Lett.,* **31**(6), L06624.

Marquering, H. & Snieder, R., 1996. Shear-wave velocity structure beneath Europe, the northeastern Atlantic and western Asia from waveform inversions including surface-wave mode coupling, *Geophys. J. Int.,* **127**(2), 283–304.

Maupin, V. & Cara, M., 1992. Love-Rayleigh wave incompatibility and possible deep upper mantle anisotropy in the Iberian peninsula, *Pure appl. Geophys.,* **138**(3), 429–444.

Maupin, V. & Park, J., 2007. *Theory and Observations—Wave Propagation in Anisotropic Media (chapter 9), Vol.1 of Treatise on Geophysics,* pp. 289–321, Elsevier, Amsterdam, The Netherlands.

Nishimura, C.E. & Forsyth, D.W., 1989. The anisotropic structure of the upper mantle in the Pacific, *Geophys. J. Int.,* **96**(2), 203–229.

Pedersen, H.A., Bruneton, M. & Maupin, V., 2006. Lithospheric and sub-lithospheric anisotropy beneath the Baltic shield from surface-wave array analysis, *Earth planet. Sci. Lett.,* **244**(3–4), 590–605.

Pegrum, R., 1984. The extension of the Tornquist Zone in the Norwegian North Sea, *Norsk Geologisk Tidsskrift,* **64**, 39–68.

Pilidou, S., Priestley, K., Gudmundsson, O. & Debayle, E., 2004. Upper mantle S-wave speed heterogeneity and anisotropy beneath the North Atlantic from regional surface wave tomography: the Iceland and Azores plumes, *Geophys. J. Int.,* **159**(3), 1057–1076.

Pilidou, S., Priestley, K., Debayle, E. & Gudmundsson, O., 2005. Rayleigh wave tomography in the North Atlantic: high resolution images of the Iceland, Azores and Eifel mantle plumes, *Lithos,* **79**(3-4), 453–474.

Ritzwoller, M.H. & Levshin, A.L., 1998. Eurasian surface wave tomography: group velocities, *J. geophys. Res.,* **103**(B3), 4839–4878.

Ritzwoller, M., Shapiro, N., Barmin, M. & Levshin, A., 2002. Global surface wave diffraction tomography, *J. geophys. Res.,* **107**(B12), 2335.

Rodi, W.L., Glover, P., Li, T.M.C. & Alexander, S.S., 1975. Fast, accurate method for computing group-velocity partial derivatives for Rayleigh and Love modes, *Bull. seism. Soc. Am.,* **65**(5), 1105–1114.

Rohrman, M. & van der Beek, P., 1996. Cenozoic postrift domal uplift of North Atlantic margins: an asthenospheric diapirism model, *Geology,* **24**(10), 901–904.

Saito, M., 1988. Disper 80: a subroutine package for the calculation of seismic modes solutions, in *Seismological Algorithms,* ed. Doornbos, D.J., Academic Press, New York, USA.

Sandoval, S., Kissling, E., Ansorge, J. & the SVEKALAPKO Seismic Tomography Working Group, 2004. High-resolution body wave tomography beneath the SVEKALAPKO array—II. Anomalous upper mantle beneath the central Baltic Shield, *Geophys. J. Int.,* **157**, 200–214.

Shapiro, N.M. & Ritzwoller, M.H., 2002. Monte-Carlo inversion for a global shear-velocity model of the crust and upper mantle, *Geophys. J. Int.,* **151**(1), 88–105.

Shomali, Z., Roberts, R. & Group, T.W., 2002. Non-linear body wave teleseismic tomography along the TOR array, *Geophys. J. Int.,* **148**(3), 562–574.

Shomali, H.Z., Roberts, R.G. & Pedersen, L.B., 2006. Lithospheric structure of the Tornquist Zone resolved by nonlinear P and S teleseismic tomography along the TOR array, *Tectonophysics,* **416**(1–4), 133–149.

Smelror, M. *et al.*, 2007. Towards a 4D topographic view of the Norwegian sea margin, *Global Planet. Change,* **58**(1–4), 382–410.

Tarantola, A. & Valette, B., 1982. Generalized nonlinear inverse problems solved using the least squares criterion, *Rev. Geophys. Space Phys.,* **20**, 219–232.

Tesauro, M., Kaban, M. & Cloetingh, S., 2008. EuCRUST-07: a new reference model for the European crust, *Geophys. Res. Lett.,* **35**, L05313.

Tomlinson, J.P., Denton, P., Maguire, P.K.H. & Booth, D.C., 2006. Analysis of the crustal velocity structure of the British Isles using teleseismic receiver functions, *Geophys. J. Int.,* **167**(1), 223–237.

Villaseñor, A., Ritzwoller, M.H., Levshin, A.L., Barmin, M.P., Engdahl, E.R., Spakman, W. & Trampert, J., 2001. Shear velocity structure of central Eurasia from inversion of surface wave velocities, *Phys. Earth planet. Int.,* **123**(2–4), 169–184.

Wessel, P. & Smith, W.H., 1998. New, improved version of the Generic Mapping Tools released, *EOS, Trans. Am. geophys. Un.,* **79**, 579.

Winchester, J.A., 2002. Palaeozoic amalgamation of Central Europe: new results from recent geological and geophysical investigations, *Tectonophysics,* **360**(1–4), 5–21.

Windley, B., 1992. Precambrian europe, in *A Continent Revealed—The European Geotraverse (chapter 6.1),* pp. 139–152, eds Blundell, D., Freeman, R. & Mueller, S., Press Syndicate of the University of Cambridge The Pitt Building, Trumpington Street, Cambridge CB2 1RP, UK.

Yanovskaya, T.B. & Kozhevnikov, V.M., 2003. 3D S-wave velocity pattern in the upper mantle beneath the continent of Asia from Rayleigh wave data, *Phys. Earth planet. Int.,* **138**(3–4), 263–278.

Yao, H., Beghein, C. & van der Hilst, R.D., 2008. Surface wave array tomography in SE Tibet from ambient seismic noise and two-station analysis—II. Crustal and upper-mantle structure, *Geophys. J. Int.,* **173**(1), 205–219.